Microwave imaging at the nanoscale: quantitative measurements for semiconductor devices, materials science and bio-applications

Ferry Kienberger, Keysight Labs Austria

This article will examine a novel high frequency electrical characterization microscope for the nano-scale imaging of semiconductor devices, advanced materials and biological samples. The scanning microwave microscope (SMM) can extract quantitative material properties at Giga-Hertz (GHz) frequencies with nanometre accuracy. The SMM interfaces two well-known measurement tools, the atomic force microscope (AFM) for materials characterisation and the vector network analyser (VNA) from telecommunication network testing for reliable microwave signal measurements. The AFM allows for nanometre lateral resolution imaging, and the VNA provides high precision impedance and admittance measurements at broadband frequencies from MHz to GHz. We give a review of this microscope including nanoscale imaging of semiconductor devices and failure analysis, as well as calibrated impedance imaging of advanced materials. Finally, we show the first calibrated complex impedance image of bacteria at 20 GHz, as well as a microwave image of a living endothelial cell acquired in liquid buffer media. This new microscope combines advanced nanotechnology imaging with microwave electronics and 3D sample modeling, for the study of advanced materials and for the first time also to bio-molecules and cells in living condition.

Introduction

The Scanning Microwave Microscope (SMM) merges the nanoscale imaging capabilities of an atomic force microscope (AFM) with the high-frequency broadband (from MHz to GHz) impedance measurement accuracy of a vector network analyser (VNA) (Figure 1). The typical frequency range of the combined SMM is between 1-20 GHz (Huber et al. 2010). It allows characterising electric and magnetic properties of materials at microwave frequencies with nanometer lateral resolution. Using the microwave signal, impedance nanoscale imaging and doping profiling of the 'Device Under Test' (DUT) can be performed. Typically the SMM is operated in reflection mode, whereby the ratio of the reflected and incident electromagnetic waves, the so called S11 scattering parameter, is measured by the VNA at each pixel of the AFM tip-sample contact point. As such a microwave image is generated pixel by pixel, simultaneously to the topographical image of the DUT. Imaging speeds are fast resulting in a typical acquisition time of one minute per image.

There are two main different imaging modes in SMM. The first is quantitative dopant profiling by means of differential capacitance (also called dC/dV), which is a widely used technique for semiconductor failure analysis and detecting leakages in solid state devices with nanometer resolution (Huber et al 2012). The dC/dV mode relies on a low frequency (kHz) modulation of the GHz S_{11} signal using the Dopant Profile Measurement Module (DPMM). It allows tuning the semiconductor depletion zone with low frequency and probing the doping concentration through the native oxide interface at GHz frequency. The second SMM mode is complex impedance imaging and it is based directly on the scattering S_{11} signal at GHz frequency (Gramse et al 2014). This complex impedance mode has been recently developed and is currently used in materials science and life science investigations. The S_{11} signal is detected by the VNA and depends on the tip-sample relative electrical impedance. A calibration workflow is required that allows converting the raw S_{11} into calibrated capacitance and resistance images of the DUT.

SMM has been extensively used to gain new insights in the semiconductor industry, and significant advances in SMM measurement and calibration

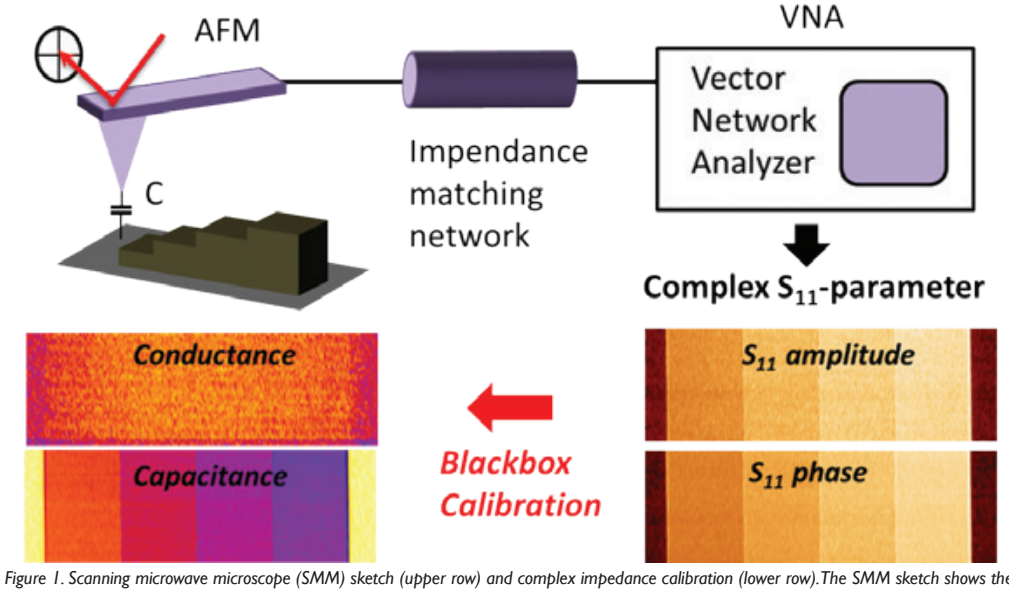

Figure 1. Scanning microwave microscope (SMM) sketch (upper row) and complex impedance calibration (lower row). The SMM sketch shows the main components including AFM cantilever with standard laser deflection readout, the impedance matching network consisting of the 50Ω shunt resistor, half-wavelength resonator and coaxial cables, as well as the VNA (vector network analyser) for GHz signal readout. The VNA measures the amplitude and phase of the complex S11 parameter, which are shown in the S11 amplitude and S11 phase images. Based on a standard VNA three error parameter black-box calibration the conductance and capacitance images are derived.

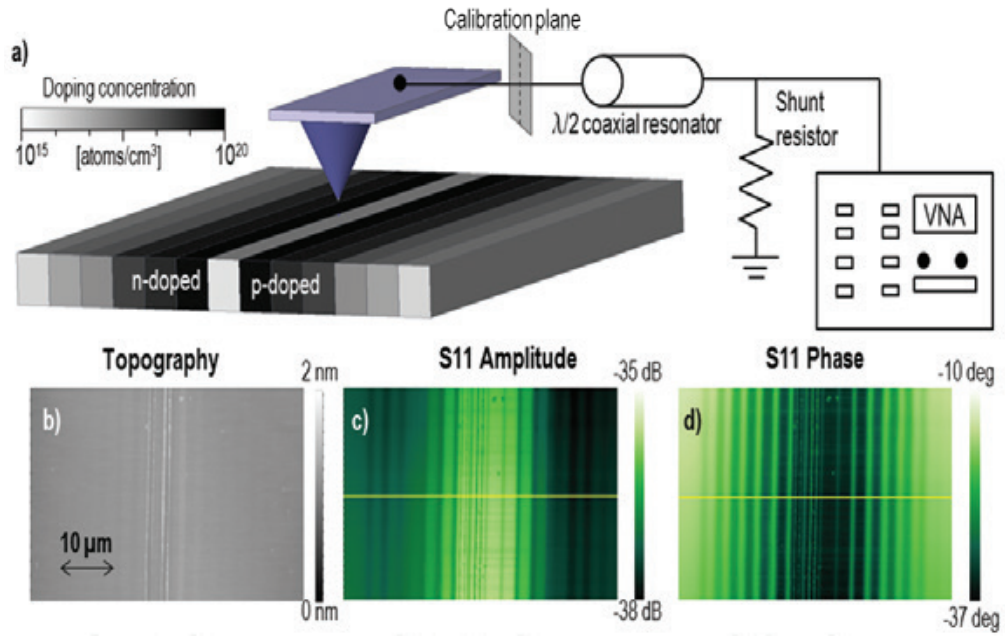

Figure 2. Sketch of the SMM experimental setup and of the doped Si sample with flat topography. The sample consists of 10 different n-implant areas and 10 different p-implant areas with a width of 2 µm each, with doping concentrations ranging from 4x1015 to 1x1020 atoms/cm3 (a). The SMM raw images of this sample are shown including flat topography (b), S11 amplitude (c) and S11 phase (d).

workflows were achieved studying well-defined semiconductor devices (Schweinboeck & Hommel 2014). Originating from the requirement of the semiconductor industry to identify failures and leakages in electronic devices with nanometer precision and low impedance values, the SMM has since proven to be a powerful tool also for materials science applications (Hoffmann et al 2014; Kasper et al 2014a). In particularly, the capability of sub-surface imaging of buried nanoscale structures has been demonstrated, as well as conductivity measurements of 2D layers (Gramse et al 2015). Recently, the high frequency characterisation of biological materials has attracted considerable interest, as SMM represents a convenient non-invasive evanescent imaging technique that complements AFM (Tuca et al 2016). While AFM measures the surface topography, the SMM can see inside materials using the electromagnetic wave penetration capabilities at GHz frequency.

In the following we present dopant profiling measurements for semiconductor device applications, complex impedance measurements for materials science investigations, and permittivity measurements of single bacteria at 20 GHz including live cell imaging in liquid media. On top of standard SMM, we present augmented SMM solutions where the standard mode is extended with other electronic measurement devices from Keysight that opens new and advanced SMM measurement capabilities. Finally, we combine SMM with the Keysight EMPro 3D modeling capabilities at GHz frequencies that can be used to calculate E-fields and complex impedance values in order to assist quantitative SMM data interpretation.

Dopant profiling and semiconductor failure analysis

For quantitative dopant profiling with dC/dV, the DPMM is attached to the VNA and a well-established calibration workflow is used that allows extracting the doping concentration of a semiconductor sample using a dopant calibration sample (Figure 2) (Huber et al 2012). The calibration workflow converts the dC/dV voltage signal to doping concentration (atoms*cm^{-3}) values. First, a calibration sample is scanned with SMM, acquiring the dC/dV image from which the dopant calibration

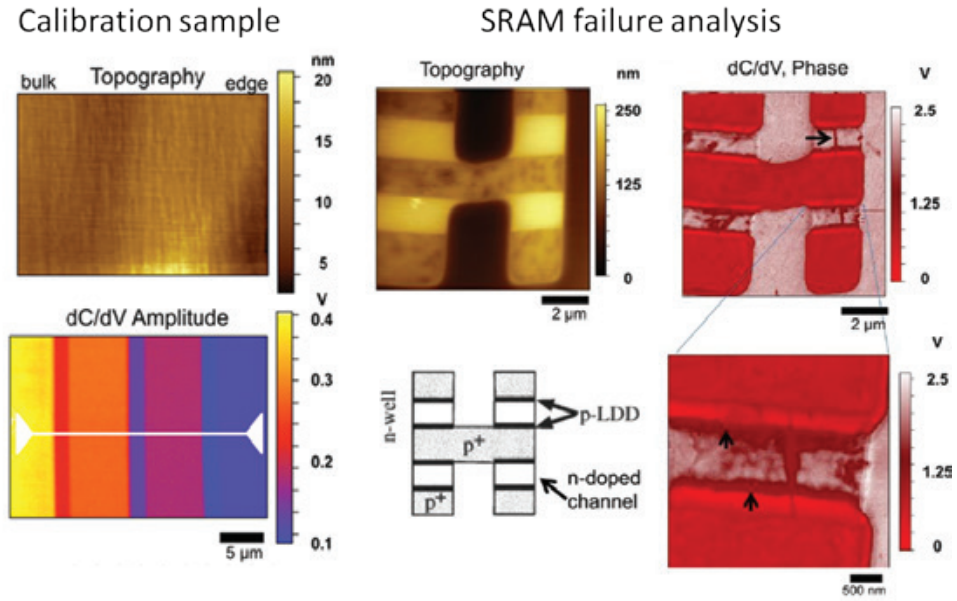

Figure 3. Dopant profiling calibration sample including topography and dC/dV image of dopant stripes (left column). Right column: imaging SRAM defect structures and p-n junctions. Topographical image with sketch of the doping polarities (left). dC/dV phase image (right column) with defect structures in the n-doped channels with a zoom in below showing p-n junctions (cf. arrow).

curve is generated (Figure 3, left column). In a second step, the dC/dV image of the DUT is acquired under the same SMM conditions. Based on the dopant calibration sample the dC/dV image of the DUT can be transferred in quantitative dopant concentrations (Schweinboeck & Hommel 2014). Figure 3 shows the application to semiconductor failure analysis. Defects or leakages on real devices can be detected using the dC/dV image which is acquired simultaneously to the topographical image, as shown on a conventional bipolar p-n SRAM sample. Several p-n defect structures within the n-doped channels can be identified in the dopant profiling image (cf. arrows in Figure 3). A sketch depicts p- and n-doped areas in Figure 3, showing a clear agreement with the various doping types and concentrations in the dC/dV image. The various regions of interest can be clearly distinguished and

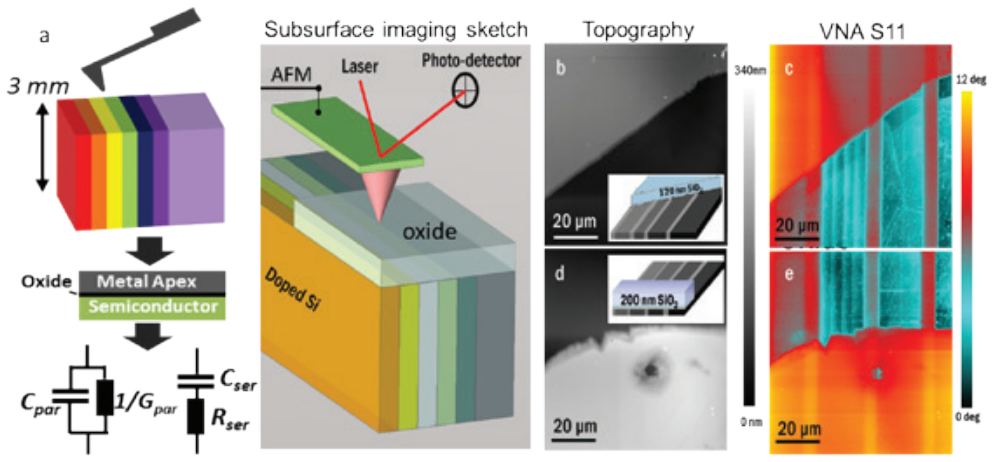

Figure 4. Sub-surface imaging. Dopant sample in cross-section with metal-oxide-semiconductor (MOS) structure and experimental setup for sub-surface imaging of a doped Si substrate partly covered with SiO2 (a). (b), (d) Topographical images of a doped Si substrate partly covered with 120 nm and 200 nm thick oxide (inset is a sketch of the sample). (c), (e) show the reflection S11 phase images with the sub-surface dopant features observed even below the oxide.

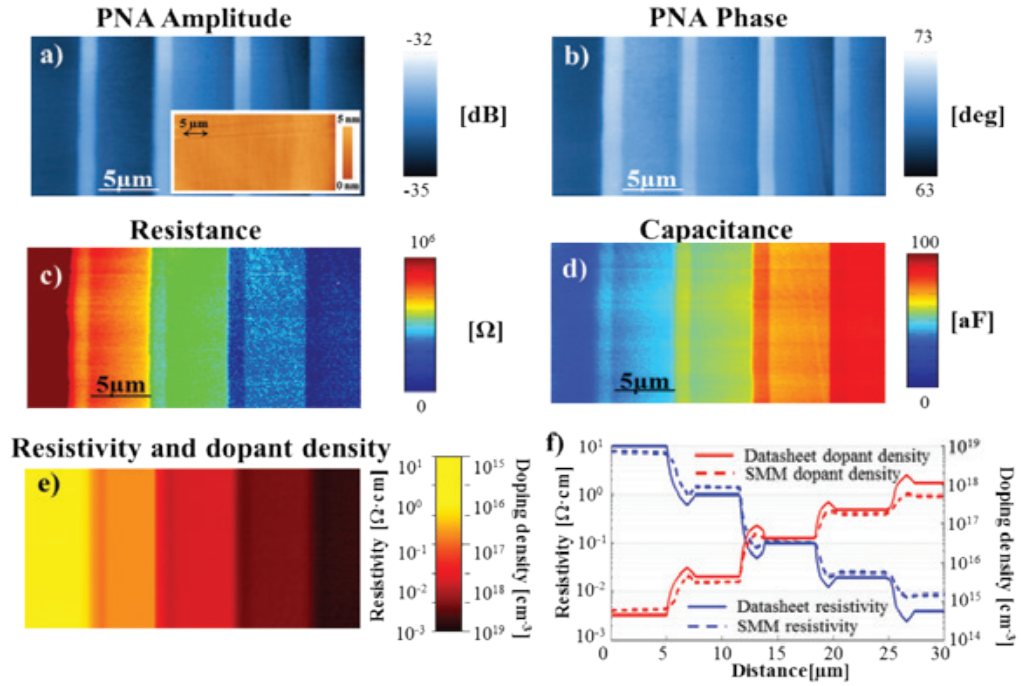

Figure 5. Calibrated capacitance and resistivity. SMM raw data (a and b) and calibrated impedance (c and d) of a n-type doped Si sample. The sample has a flat topography (inset in a) and different n-doped areas with doping concentrations. The 5 µm wide doping areas are separated by 1 µm wide bulk interface layers. The resistivity and doping concentration (e) are calculated from the SMM resistance. (f) Comparison with data sheet.

the doping polarity and density analysed. No cross talk is obtained between topography and dopant profiling image. Bipolar p/n junction interfaces are observed with a width of 100 nm. The exact width of the p-n junction depends on the SMM tip voltage bias that can be further used to investigate the physics of the depletion zone interface.

Sub-surface imaging: seeing below the surface

Figure 4 shows that SMM can use the penetration capabilities of GHz microwaves to perform non-destructive in-depth imaging of structures located underneath the sample surface (Gramse et al 2015). This capability, named as sub-surface imaging, is an important benefit when the area of interest is buried under the sample surface. Figure 4 (left column), shows a silicon test sample with varying dopant density (10^{15}–10^{19} atoms*cm^{-3}) where the calibrated impedance can be determined from the SMM images. The right column shows the sub-surface imaging proof and concept. The dopant sample is covered with dielectric layers of SiO_2 (100–400 nm thickness). SMM, with a noise level of 1 aF, allows sensing the electrical properties of doped silicon structures buried under oxides with more than 400 nm thickness. SMM can be therefore used to accurately perform quantitative nanoscale probing of dielectric materials and to perform calibrated capacitance characterisation of buried structures. This finds applications in the field of semiconductor failure analysis studies including process optimizations for integrated chip fabrication.

Calibrated capacitance and resistivity: quantitative materials properties from SMM

Based on the S_{11} complex impedance calibration workflow, the SMM images are converted into capacitance and resistance (Figure 5) (Gramse et al 2014). Using a tip–sample analytical model that includes tip radius, microwave penetration skin depth, and semiconductor depletion layer width, the resistivity of the DUT can be extracted from the

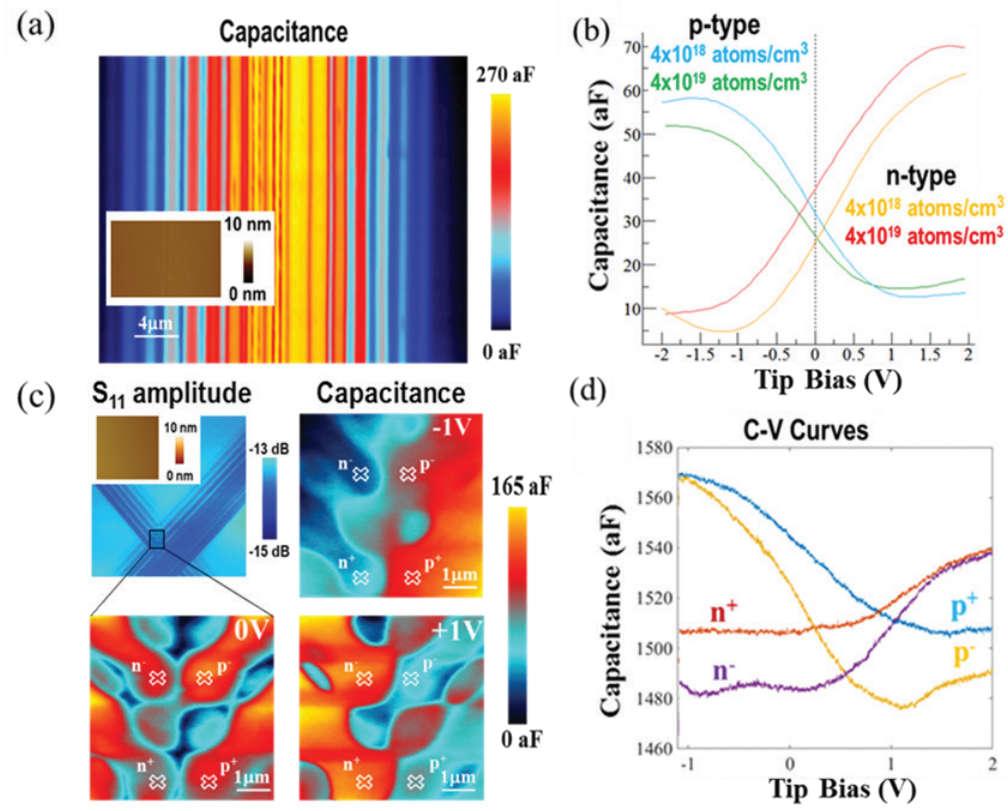

Figure 6. Capacitance-voltage (C-V) spectroscopy experiments. (a) Calibrated capacitance and topography (inset), of a bipolar doped Si staircase sample with n- and p-implanted areas. (b) C-V curves generated from the image acquired at different tip-bias voltages. (c) S11 amplitude with topography (inset), and zoomed-in calibrated capacitance of a flat p-n junction structure. The three capacitance images have been acquired at -1V, 0V, and +1V tip bias, respectively. (d) Pointwise C-V spectroscopy curves in the four different spots labeled with crosses in (c).

calibrated SMM resistance as recently demonstrated (Brinciotti et al 2015). The method has been tested on two doped silicon samples and in both cases the resistivity and doping concentration are in quantitative agreement with the data-sheet values over a range of 10^{-3} Ω cm to 10^{1} Ω cm, and 10^{14} atoms cm^{-3} to 10^{20} atoms cm^{-3}, respectively (Figure 5). The method does not require sample treatment like cleavage and cross-sectioning, and high contact imaging forces are not necessary, thus it is easily applicable to various semiconductor and materials science investigations. In Figure 5, the calibrated resistance and capacitance images show lower and higher values for the highly doped areas, respectively. Using an analytical method the SMM resistance image can be converted into a resistivity and dopant density image, which are true materials property images. Figure 5 compares the SMM resistivity and doping concentration with the data-sheet values of the sample; a quantitative agreement is obtained for the entire range of doping concentrations. The lateral resolution of SMM is limited by the AFM tip probe apex radius while the bulk penetration is mainly determined by the skin-depth. The skin depth and therefore the microwave penetration depth can be changed by varying the SMM frequency. In this way, frequency dependent depth profiling can be realized with the SMM.

Capacitance-voltage spectroscopy for further physics investigations

The nanoscale lateral resolution of SMM allows performing imaging of doped regions, interfaces, and junctions that often play a critical role in several semiconductor devices. Figure 6 shows a bi-polar

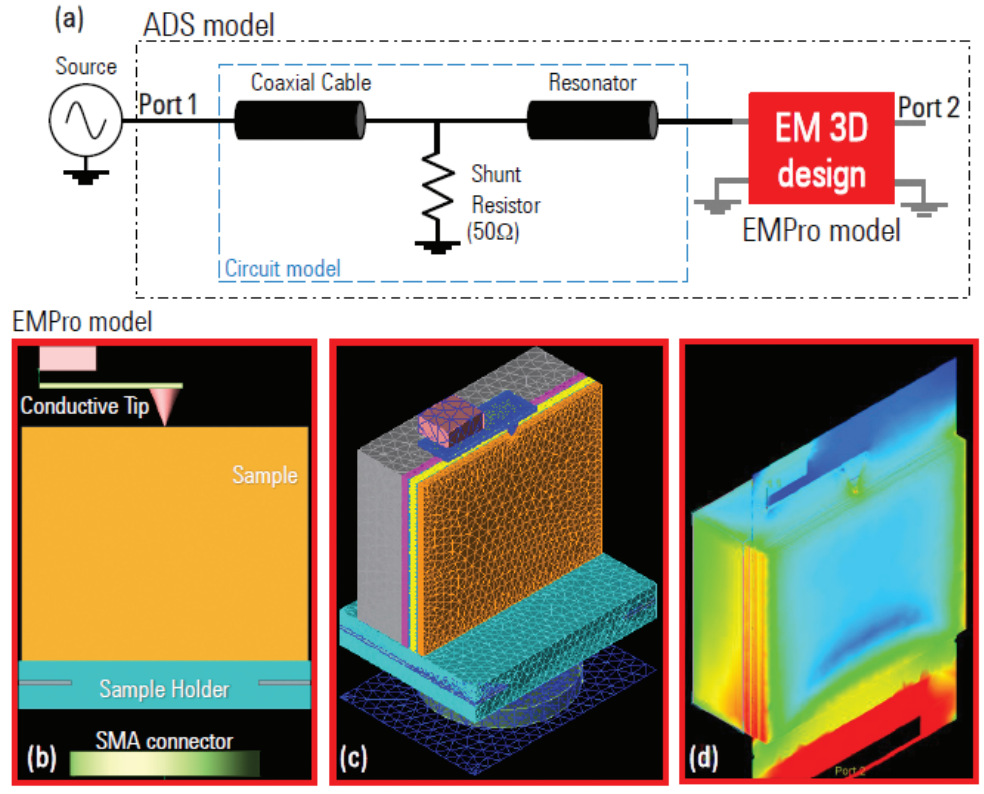

Figure 7. SMM modeling with ADS and EMPro. (a) Integrated 2D circuitry model (ADS) and 3D EM design block (EMPro model). (b) 3D CAD model of the cantilever and sample holder. (c) Meshed view in EMPro advanced mode. (d) E-Field distribution at 10 GHz.

doped silicon sample imaged with SMM to obtain calibrated capacitance images at different tip DC-voltage bias (Brinciotti et al 2016). The capacitance depends on the doping density and reaches up to 300 aF, with high capacitance values observed on highly doped silicon regions. The same area was imaged with different DC tip-bias voltages between -2V and +2V. By plotting the calibrated capacitance versus the tip-bias voltage the C-V curves can be generated for different locations. The conductive AFM-tip and the thin native silicon dioxide layer (~1 nm) with the doped silicon substrate below form a Metal-Oxide-Semiconductor (MOS) structure. In this configuration, for n-type doped silicon regions, an increase in capacitance at high positive voltages is measured, which is in line with the standard depletion zone model. The C–V curve for the p-type stripes shows high capacitance values at negative tip bias and low capacitance at positive tip bias which follows also the textbook model. A second region of interest on the same silicon sample includes multiple p-n junction structures. The topography of the area is flat, and the structures are only visible in the electrical SMM images. Also in this case, the same area has been imaged multiple times in different DC tip bias conditions. From the capacitance images the different polarity of the n-type and p-type region can be determined. These results show that the C-V curves can be either determined pointwise at particular positions or also from the entire capacitance image acquired at different DC tip-bias voltages (Moertelmaier et al 2014).

Nanoscale modeling with ADS and EMPro: GHz electric field distribution

Calibrated SMM experiments can be compared to quantitative modelling using two software

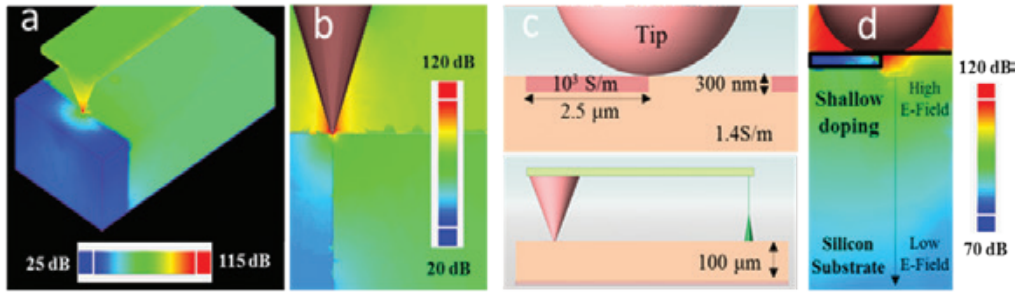

Figure 8. Nanoscale EMPro modeling. (a) 3D E-field distribution of the tip-sample system. The E-field is lower in the doped region with high-conductivity (shown in blue), than in the Si bulk of the sample (shown in green). (b) Cross-section of the 3D E-field distribution. (c) EM-Pro model geometry (bottom), with a zoom on a shallow doped structure (top). (d) Cross-section of the E-field distribution showing the tip-sample region. The E-Field is highest close to the tip and decreases inside the sample.

packages, ADS and EMPro (Figure 7) (Kasper et al 2014b; Medina et al 2015). ADS is an electric circuit simulation tool that provides optimisation, tuning, network parameters, and the broadband frequency response for standard electronic components. ADS was used to model the broadband frequency S_{11} response of the coaxial cables and the impedance matching network, as well as the effect of the AFM tip in contact with different materials samples. The ADS frequency sweep simulations were compared to experimental SMM data and a quantitative agreement has been achieved. With the 3D modeling tool EMPro, calibrated SMM impedance images and electrical E-field distributions can be compared to 3D microwave finite element modelling. As such, 3D electromagnetic full-wave simulations using EMPro can validate the calibrated complex impedance SMM measurements (Figure 7). EMPro supports two simulation engines, Finite Element Modelling (FEM) and Finite Difference Time Domain (FTDT). In FEM, the structure is included in CAD (Computer Aided Design) and meshing is done until the solutions for the Maxwell's equations in the mesh tetrahedrons converge to a certain threshold. Integrating the obtained electric and magnetic fields, the voltage and current is calculated in each mesh point. The ratio of voltage to current calculated by EMPro at the port gives the impedance, which corresponds to S_{11}. Both EMPro and ADS modelling are used to gain insights into the sub-surface imaging

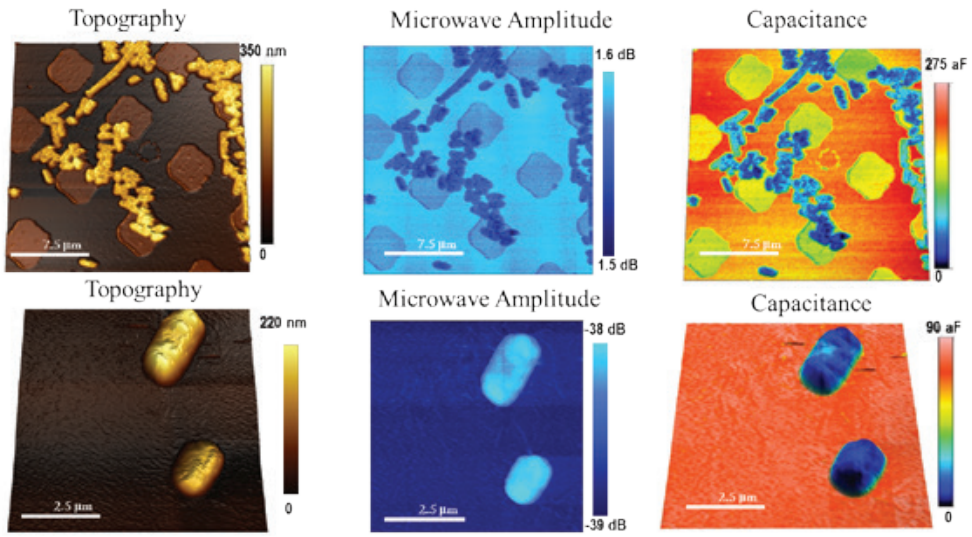

Figure 9. GHz image of single bacteria. Multitude of E. coli bacteria imaged with the SMM in air. The first column shows the AFM topography image, the second column shows the raw SMM S11 image. The last column shows the calibrated capacitance map overlaid on the 3D topography image.

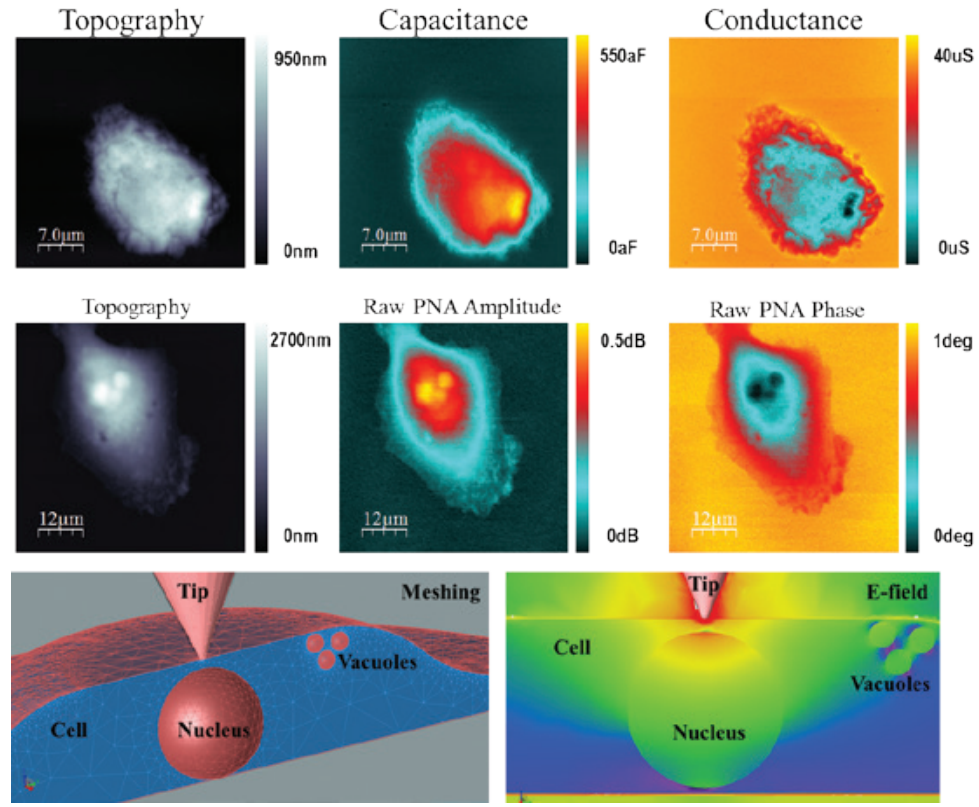

Figure 10. Upper row: Cell complex impedance imaging in air and liquid. Individual CHO (Chinese Hamster Ovary) cell imaged in air in intermittent contact mode showing topography, calibrated capacitance and conductance. Centre row: SMM images of individual ARPE-19 (Arising Retinal Pigmented Epithelia) cell fixed on Si++/SiO2 substrate and imaged in liquid solution of medium, serum, and antibiotics. Lower row: Tip-cell interaction with 3D EMPro model mesh of the cantilever, tip, cell and Si substrate (left). EMPro simulation of E-field over cell surface and penetration into the cell (right).

capabilities of oxides and semiconductor materials at different frequencies and different experimental conditions. As such the modelling packages are useful for proper experimental SMM planning as well as further data interpretation at a quantitative level (Oladipo et al 2013).

Figure 8 shows how the 3D-field solver EMPro was used for nanoscale modeling of the E-field and impedance values of the SMM tip-sample system at 19 GHz (Brinciotti et al 2016). Figures 8a and 8b show a 3D distribution of E-field magnitude at the tip-sample system on the interface between two doped silicon regions having different doping concentrations. This geometry model describes, in a simplified way, the structure of the uni-polar n-type doped calibration sample, where the differently doped regions extend over the entire sample thickness. The E-Field has a maximum, as expected, near the very end of the conductive tip. The part of the sample where the field is low (shown in blue in the color map), corresponds to the region with higher doping concentration. Accordingly, the field is higher (shown in green), in the region with lower conductivity (i.e. lower doping concentration). The modeling of the bulk sample was compared with a shallow doped sample where the doping extends only within few hundreds of nanometers from the sample surface (Figures 8c and 8d). For this reason a different CAD geometry has been designed to model the shallow stripes which are 300 nm high and 2.5 µm wide, with a conductivity of 1000 S/m. Figure 8d shows a cross-section of the tip-sample E-field distribution. The E-Field has a maximum close to the SMM tip, decreasing proportionally to the depth in the bulk region, whereas it reaches a relative minimum value inside the shallow doped

stripe, which is 300-nm thick. The penetration depth of the E-field is roughly half a micrometer into the sample, which is comparable with the doping depth.

GHz images of single bacteria: capacitance and complex permittivity

The SMM was used to measure *Escherichia coli* (*E. coli*) bacteria in air and in liquid using intermittent contact mode for imaging soft materials (Figure 9) (Tuca et al 2016). Quantitative SMM calibration is achieved resulting in complex impedance images of bacteria in air including capacitance (aF; attoFarad) and conductance (μS; microSiemens) images. *E. coli* bacteria were immobilised onto a silicon substrate and imaged with the SMM either in the dry state or in buffer solution. Figure 9, upper row, shows an ensemble of bacteria spread over the surface of Si and SiO_2 pillars while the lower row shows two individual bacteria on Si. The topography images show *E. coli* bacteria with lengths of 2-3 μm and a height of 300-350 nm. The SMM raw data includes the VNA amplitude image showing a good contrast between the bacteria, SiO_2 pillars and the Si substrate. The calibrated capacitance images show individual bacteria with a capacitance ranging from 20-100 aF depending on the tip diameter and the frequency. The capacitance of the bacteria as well as the SiO_2 pads is lower than the capacitance of the substrate. This is consistent assuming a simple parallel plate capacitor model where the capacitance decreases with increasing distance of the tip and the substrate. The conductance channel shows no variation between bacteria and substrate (data not shown), which is expected from the non-conductive SiO_2 pads and indicates that the bacteria have no electrical loss under the measurement conditions. In a subsequent study we quantified the electric permittivity of single bacterial cells at microwave frequencies and nanoscale spatial resolution by means of near-field scanning microwave microscopy (Biagi et al 2016). To this end, calibrated complex impedance and admittance images have been obtained at 19 GHz and analysed with a methodology that removes the non-local topographic cross-talk contributions and thus provides quantifiable intrinsic dielectric images of the bacterial cells. Results for single *Escherichia coli* provide a relative electric permittivity of ~4 in dry conditions and ~20 in humid conditions, with no significant loss contributions. Present findings, together with the ability of microwaves to penetrate the cell membrane, open an important avenue in the microwave label-free imaging of single cells with nanoscale spatial resolution.

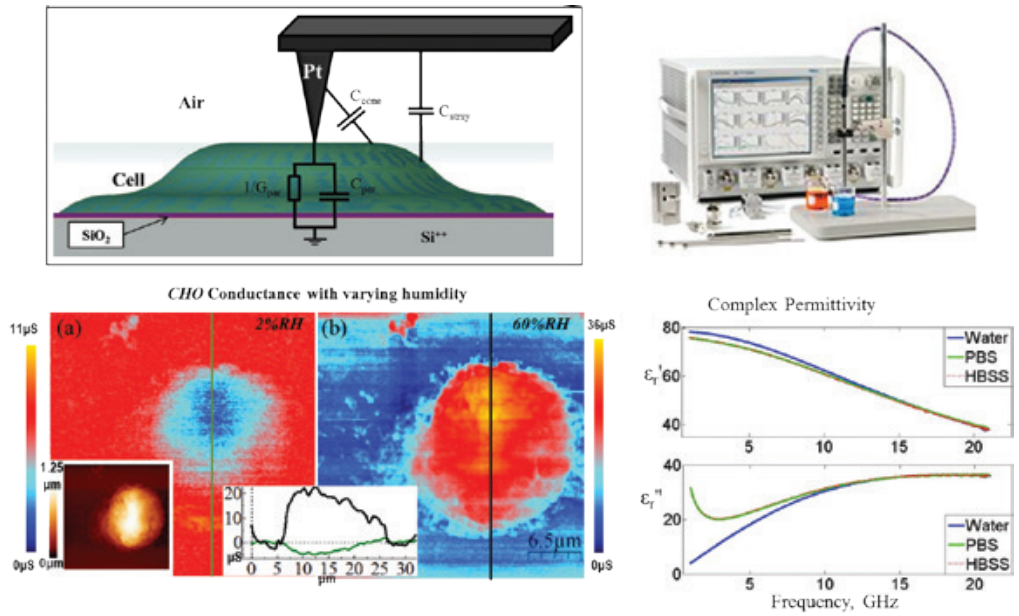

Figure 11. Cell conductivity at different humidity. SMM equivalent electric circuit model of the tip-cell interaction (upper left). Calibrated cell conductance images measured at different ambient humidities (lower left). Inset shows cell topography. Real and imaginary parts of water complex permittivity, 0.1M PBS and HBSS buffers as a function of frequency, over the range 1-20GHz (lower right), experimentally obtained using VNA and dielectric slim probe kit from Keysight (upper right).

Cell conductivity at humidity and living cell imaging at GHz frequencies

Figure 10 shows the topography and calibrated capacitance and conductivity images of single Chinese Hamster Ovary (CHO) cells acquired in air (upper row) and in liquid (middle row; living cell) (Tuca et al 2016). Due to their large dimensions, they can be easily spotted on the silicon substrate and individually scanned in contact mode. The topography images show a diameter of roughly 30μm and a height of more than 1μm. The obtained capacitance variation is induced by cell dielectric properties that are different from the Si substrate dielectric properties. Figure 10, lower row, shows the microwave interaction at the tip/sample contact point using EMPro. A 3D cell-like structure has been implemented in CAD including the cell nucleus, three vacuoles, and a 10nm thick membrane. The simulated values of admittance were obtained at different frequencies and positions over the cell, in order to investigate how different cell compartments influence the electric field distribution. Different dielectric values were used for the individual cell compartments including the lipid bilayer of the cell membrane (ε_r=3.2), the cell nucleus with DNA (ε_r=8) and a protein vacuole (ε_r=3). Depending on the cell and tip geometry, the simulated tip-cell complex admittance was determined as roughly Y=110 + j250 μS, which translates to conductance values of roughly 50 μS and capacitance values of 500 aF. Those modeled EMPro values fit very well to the experimental SMM results. Figure 11 shows a set of CHO cell measurements with controlled variation of the ambient humidity, ranging from low humidity (2% RH) to high humidity (60% RH). The calibrated conductance values obtained at low humidity are in the order of 10-20 μS, whereas the values obtained at high humidity vary between 30-200 μS, which can be explained with the variation of the conductivity based on the water content in the cells.

Figure 11 shows the variation of the complex permittivity of different aqueous solutions (pure water, PBS, and HBSS) with respect to frequency ranging from 1-20GHz, recorded with the dielectric probe kit (Tuca et al 2016). The choice of the three solutions should match the cell buffer solutions. The real part of the water dielectric constant thereby decreases from =78 at 2GHz to =40 at 20GHz. The imaginary part of the water relative permittivity is proportional to the conductivity , based on , where is the permittivity of free space, and f is the frequency. The dielectric probe measurements reveal a low value of the imaginary part of the relative permittivity (<10, <1S/m) at low frequency (2GHz) and a high value (=35, =40S/m) at high frequency (20GHz). The SMM cell conductivity can now be compared to the water conductivity at 20GHz. The SMM conductivity σ can be obtained from the conductance G in a simple first order approximation from the volume of the cell in contact with the SMM tip, and applying the relation , where *A* is the contact area and *l* is the cell height obtained from the topography image. The effective conductivity obtained from the SMM cell conductance, at f=20GHz, is =18 S/m and effective =15, which is in the range of the bulk water permittivity. Accordingly, the cell conductivity behaviour at different frequencies and ambient humidity is similar to bulk water properties, corroborating the hypothesis that water is adsorbed on the cells' surface and that it is responsible for the microwave energy dissipation over the cells.

Summary

The Keysight Scanning Microwave Microscope (SMM) consists of an AFM interfaced with a vector network analyser (VNA) allowing measurement of complex materials properties for nano-electronics,

materials science, and life science applications. The SMM operates at broadband frequencies between 1-20 GHz. We present novel calibration workflows for complex impedance imaging and dielectric quantification, as well as advanced voltage-spectroscopy measurements. Various nanodevices are studied including dopant profiling layers, semiconductor devices, buried oxide structures, and biomaterials like cells and bacteria. Due to the capability of the electromagnetic wave to penetrate the surface of the sample under study, the technique can be used to selectively image sub-surface features. Calibrated sub-surface and non-contact capacitance imaging of silicon samples is presented and dopant areas can still be detected under a silicon oxide layer. Finally, SMM imaging in buffer solution is presented including life cell imaging, and complemented by 3D EMPro modeling at GHz frequencies.

References

Biagi, M.C. et al. (2016), "Nanoscale Electric Permittivity of Single Bacterial Cells at Gigahertz Frequencies by Scanning Microwave Microscopy," ACS Nano, 10 (1), 280-288.

Brinciotti, E. et al. (2015), "Probing resistivity and doping concentration of semiconductors at the nanoscale using scanning microwave microscopy", Nanoscale, 7, 14715-22.

Brinciotti, E. et al. (2016), "Frequency analysis of dopant profiling and capacitance spectroscopy using Scanning Microwave Microscopy", submitted.

Gramse, G. et al. (2014), "Calibrated complex impedance and permittivity measurements with scanning microwave microscopy", Nanotechnology 25, 145703-11.

Gramse, G. et al. (2015), "Quantitative sub-surface and non-contact imaging using scanning microwave microscopy", Nanotechnology 26, 135701-10.

Hoffmann, J. et al. (2014), "Measuring Low Loss Dielectric Substrates with Scanning Probe Microscopes," Applied Physics Letters, 105, 013102-6.

Huber, H.P. et al. (2010), "Calibrated nanoscale capacitance measurements using a scanning microwave microscope", Rev. Sci. Instr. 81, 113701-9

Huber, H.P. et al. (2012), "Calibrated nanoscale dopant profiling using a scanning microwave microscope", J. Appl. Phys. 111, 014301-9.

Kasper, M. et al. (2014a), "Metal-oxide-semiconductor capacitors and Schottky diodes studied with scanning microwave microscopy at 18GHz", J. Appl. Phys. 116, 184301-8.

Kasper, M. et al. (2014b), "Electromagnetic Simulations at the nanoscale: EMPro modeling and comparison to SMM experiments", Keysight Application Note 5991-2907EN.

Medina, P.F. et al. (2015), "Transmission and reflection mode scanning microwave microscopy (SMM): experiments, calibration, and simulations", Proceedings of the 45th European Microwave Conference, Paris, 654-657.

Moertelmaier, M. et al. (2014), "Continuous capacitance–voltage spectroscopy mapping for scanning microwave microscopy", Ultramicroscopy 136, 67–72.

Oladipo, A. O. et al. (2013), "Three-dimensional finite-element simulations of a scanning microwave microscope cantilever for imaging at the nanoscale", Appl. Phys. Lett. 103, 213106-10.

Schweinböck, T. & Hommel, S. (2014), "Quantitative Scanning Microwave Microscopy: A calibration flow", Microelectronics Reliability, 54, 2070–4.

Tuca S.S. et al. (2016), "Calibrated complex impedance of CHO cells and E. Coli bacteria at GHz frequencies using scanning microwave microscopy," Nanotechnology, 27, 135702-11.

Acknowledgements

The authors would like to thank Manuel Kasper, Enrico Brinciotti, Giorgio Badino and Michael Dieudonne from Keysight Technologies; Georg Gramse, Silviu Tuca and Peter Hinterdorfer from Johannes Kepler University of Linz; Gabriel Gomila and Maria Chiara Biagi from IBEC Barcelona; Juergen Smoliner from TU Vienna. This work has been supported by EU-FP7 (PEOPLE-2012-ITN-317116, NANOMICROWAVE) and Austria Bio-SMM FFG (Project No. 846532).

Biography

Ferry Kienberger is the SMM group leader at Keysight Labs Linz. He obtained the PhD in 2002 in Technical Physics at JKU Linz with subsequent Postdoctoral stays in Bioinformatics and Biophysics at University of Salzburg and Linz. In 2007 he joined the central cooperate research lab of Agilent Technologies. The work included research in nano-biotechnology and measurement electronics including high frequency microwave applications. After the split of Agilent Technologies in 2014 he is member of the central research lab of Keysight Technologies and head of the Keysight research lab in Linz. Keysight is a leading test and measurement company headquartered in Santa Rosa, California, with 10.000+ employees. Corresponding Author Details: Dr Ferry Kienberger, Keysight Technologies Austria GmbH, Keysight Labs Linz, Gruberstrasse 40, A-4020, Linz, Austria. email: ferry_kienberger@keysight.com